Design and modelling of a reversible shape memory alloy torsion hinge actuator

Liu, Qiang; Ghodrat, Sepideh; Jansen, Kaspar M.B.

DOI
10.1016/j.matdes.2023.112590

Publication date
2024

Document Version
Final published version

Published in
Materials and Design

Materials & Design 237 (2024) 112590

Contents lists available at ScienceDirect

Materials & Design

journal homepage: www.elsevier.com/locate/matdes

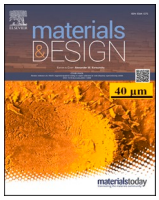

Design and modelling of a reversible shape memory alloy torsion hinge actuator

Qiang Liu *, Sepideh Ghodrat, Kaspar M.B. Jansen

Emerging Materials Laboratory, Department of Sustainable Design Engineering, Faculty of Industrial Design Engineering, Delft University of Technology (TU Delft), Landbergstraat 15, 2628 CE Delft, The Netherlands

ARTICLE INFO

Keywords:
Shape memory alloy
Nitinol
Torsion deformation
Reversible hinge actuator
Phenomenological model

ABSTRACT

Conventional hinge actuators often face limitations including excessive weight, large size and unpleasant noise. Shape memory alloys (SMAs) offer a solution to address these issues due to their favorable characteristics, such as lightweight, high actuation force and small form factor. However, most existing SMA-based hinge actuators rely on the tension loading mode. Achieving an ideal actuation angle thereby necessitates the inclusion of long SMA wires, which inadvertently constrains the actuator size. Notably, the full potential of SMAs' deformation capacities, encompassing torsion and bending, remains largely untapped and underutilized.

In this research, a reversible torsion SMA hinge actuator is studied, which can reversibly open 60° during heating and cooling. The actuator weighs 2 g, and can produce actuation forces of up to 5 N. The mechanical performances of nitinol at different temperatures are measured. Based on the measurements, a model which can predict the opening and closing angle is proposed, with deviations of 13.5 ± 8.2 %. Gripper and butterfly demonstrators constructed by the hinge actuators are given as application examples. The actuators hold potential in many fields like soft robotics, aerospace and medical instruments.

1. Introduction

Mechanical actuators serve to transform various types of input energy into mechanical motion [1]. During the 1960 s and 1970 s, early iterations of these devices predominantly featured arm-like manipulators that employed electric motors or pneumatic and hydraulic actuators [2]. Despite offering benefits such as precise control and high actuation force, conventional actuators are often bulky, expensive and noisy, thus constraining their application scenarios. In addition, pneumatic and hydraulic actuators necessitate frequent maintenance due to their sensitivity to contamination [2]. To develop portable, lightweight, and adaptive devices, some researchers are exploring the integration of smart materials into mechanical actuators [3]. Recent advancements include the applications of shape memory alloys (SMAs) and shape memory polymers (SMPs). These materials have numerous advantages, including lightweight, small form factor, simple structure, and wide selection of actuation force [2,4–6].

Hinges and rotary joints, as prevalent forms of mechanical actuators, find widespread application in various fields, such as foldable mechanisms for industrial manipulators and robotics. Smart materials have been used to exploit smart hinges in some research. For example, Yamamura *et al.* proposed a large-deformation hinge that combines shape memory polymer with a soft elastomer [7]. More studies on shape memory polymers and their composites indicate promising applications in areas like packaging [8], solar arrays [9] and assembly structures [10]. SMP-based hinges offer the advantages of being lightweight and capable of large deformation, but they produce low actuation force, and need additional heating circuits or other types of external stimulus [4].

Shape memory alloys are a type of smart materials which can recover to their pre-trained shapes upon heating. They have been used in a variety of fields including aerospace [11,12], medical [13,14] and smart wearables [15–17]. SMAs present an option for creating lightweight hinges with small form factors and high actuation forces. Pre-stretched SMA wires can generate 4–8 % of shrinkage as well as a relatively high actuation force when heated. Some researchers take the advantage of this property to develop tension-driven hinges [4,18,19]. Typically, such hinges are composed of SMA wires, rigid parts and strip-shape rubbery elements (see Table S1 and Fig. S1 (d) in supplementary information). The length of the SMA wires significantly affects the bending angles of the tension-driven hinges. Owing to the limited contraction strain of the SMAs, these hinges are often designed to be thin and strip-like (e.g. 20 cm long) to accommodate enough wire length. Additionally,

* Corresponding author.
E-mail address: q.liu-6@tudelft.nl (Q. Liu).

https://doi.org/10.1016/j.matdes.2023.112590
Received 16 October 2023; Received in revised form 27 November 2023; Accepted 15 December 2023
Available online 18 December 2023

some researchers developed bending-driven hinges based on the bending deformation of SMA [20–22]. Bending-driven hinges that use large-diameter SMAs can be engineered with a compact form factor while delivering substantial actuation force. However, to prevent fracture at the bending position, the SMA wires or plates must be bent with a larger radius, which consequently results in increased hinge thickness. Torsion-driven hinges represent another category of hinges that exploit the torsional deformation properties of SMAs. These hinges are compact and capable of generating high actuation forces. Related research can be found in [23]. More details of the three categories of SMA-based hinges are provided in the supplementary information.

A reversible torsion SMA hinge actuator is investigated in this paper. As depicted in Fig. 1, the hinge comprises two nitinol wires. The first wire (SMA, coloured blue) acts as the actuator wire and has an initial training angle of 180°. The second wire is a superelastic wire (SE, coloured red, pre-trained angle 0°) which supplies the antagonist force. Superelastic materials are SMAs which are already actuated at room temperature. When an SMA wire and an SE wire are combined at room temperature, the hinge finds an equilibrium position with an angle somewhere close to the SE's original angle (denoted as θ_{min} in Fig. 1). When the actuator hinge is heated above the SMA's transition temperature, SMA is actuated, driving the hinge toward its pre-trained angle (180°), and balance with the SE wire at θ_{max}. Therefore, throughout the heating and cooling cycles, the actuator hinge can repeatedly alternate between two pre-set actuation angles. The actuation span $\Delta\theta$ is defined as the difference between the θ_{max} and θ_{min}.

The proposed hinge actuator in this paper is a torsion-driven hinge, where the actual deformation occurs in the torsion part as illustrated in Fig. 1. Koh *et al.* presented a similar configuration, comprising two pre-trained SMA wires [23]. By alternately activating the two SMA wires, the desired hinge deformation can be achieved. They also proposed a constitutive model based on the model of Liang *et al.* [24] to predict the angle-torque relationship. This model involves complex molecular-level parameters such as the thermodynamics of nucleation, critical strains and transformation tensors [25], which makes it less practical to apply. Compared to using two SMA wires, the reversible torsion hinge actuator presented in this article consumes less energy, because it does not require additional heat sources for shape recovery. In addition, the two wires overlap and are situated in the pivoting line, resulting in a hinge structure with an extremely small form factor.

In this article, we develop a lightweight reversible torsion hinge actuator which requires a single heating source, and propose a phenomenological model to predict their actuation angles based on given material properties and geometric parameters. The influences of the SMA pre-trained angle and torsion length on the hinge actuation angle are investigated. The structure of this paper is organized as follows: Sections 2 and 3 detail the materials and testing methods, while section 4 presents an analysis of the experimental results. A model of the SMA-based torsion hinge actuators is proposed in section 5, followed by a validation study in section 6. Finally, the influences of SMA pre-trained geometric conditions on the hinge actuator angles are discussed and application examples are demonstrated in the discussion section 7.

2. Materials and configuration

2.1. Materials

1.00 mm diameter nitinol wires (55.59Ni-44.41Ti wt%) purchased from Nanografi Nanotechnology are used in the experiments. The alloy's documented austenite finish temperature spans from 45 ℃ to 50 ℃. Additionally, 0.75 mm diameter superelastic wires produced by Kellogg's Research Labs are employed with an equal weight percentage of 50.00 for both nickel and titanium. The reported austenite finish temperature for these superelastic wires is 20 ℃.

2.2. Configuration of torsion tests

A TA instrument Dynamic Mechanical Analyser (DMA) Q800® is used for the torsion tests. The SMA wire bending process of a nitinol wire is depicted in Fig. 2(a). After annealing for 30 min in an oven at 550 ℃, a hinge-shape specimen is acquired. To transform the uniaxial motion of the Q800 device into torque deformation, a special tool is constructed consisting of the SMA wire, aluminium tabs and a rod (Fig. 2(b)). During extensional loading of the tabs, the *torsion part* of the SMA is loaded in torsion deformation. The configuration needs to be lubricated to reduce friction between the nitinol wire and aluminium structures before each test, and the setup is used in tests of section 3.3 and 3.4.

3. Testing methods of SMA and SE

3.1. Transformation temperature tests

Differential Scanning Calorimetry (DSC) is used to determine the transformation temperatures of the SMA and SE materials. To obtain a larger contact surface between the nitinol wire and aluminium pan, the wire is flattened using a hammer. Subsequently, the nitinol wire undergoes annealing in a 550 ℃ oven for 30 min and are then quenched in cold water [26].

A TA instrument Differential Scanning Calorimetry Q2000® is used for transformation temperatures assessments. Prior to testing, a 16.33 mg SMA specimen is placed into a Tzero® aluminium pan with a lid, weighing 50.72 mg. An empty aluminium pan (50.87 mg) serves as the reference. The testing procedure is programmed as follows: initially, the temperature is equilibrated at −60 ℃ and held isothermal for 2 min. It

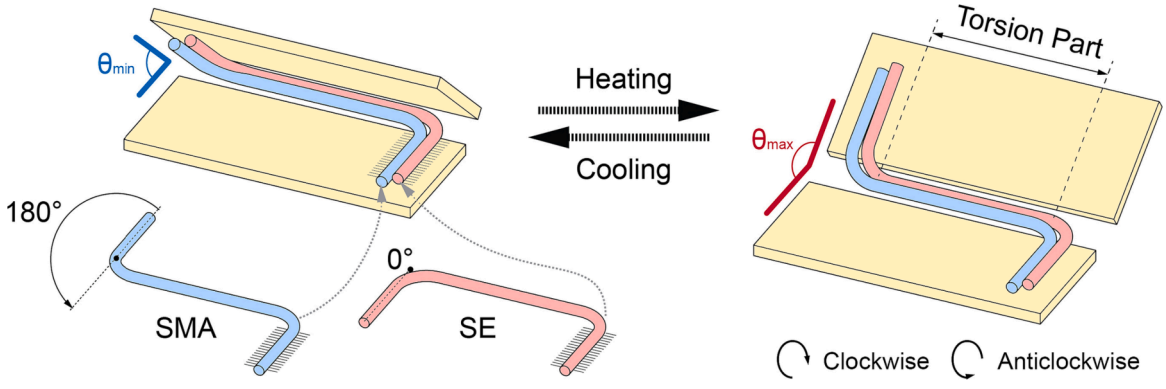

Fig. 1. Configuration of the reversible torsion SMA hinge actuator. The blue wire represents the SMA wire, while the red wire corresponds to the superelastic wire. The hinge leaves are coloured yellow. 180° and 0° represent the pre-trained angle of SMA and SE respectively. θ_{min} and θ_{max} is the hinge angle at cold and heated states correspondingly. (For interpretation of the references to colour in this figure legend, the reader is referred to the web version of this article.)

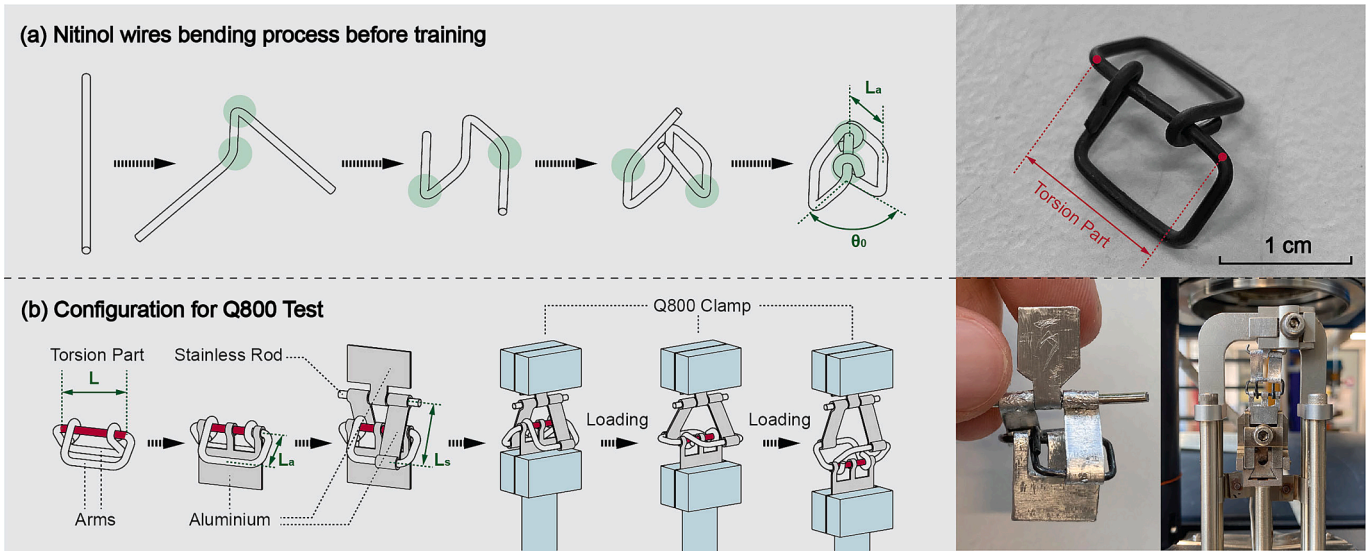

Fig. 2. Construction of the tool for torsion tests on nitinol wires. (a) Bending process before SMA training. The green areas are the bending positions. (b) Configuration process for Q800 tests. The red areas are the SMA torsion deformation parts. The blue structures are the Q800 clamps. L is the length of the SMA torsion part. L_a is the length of the SMA arm. θ_0 is the initial angle between the two arms. L_s is the length of the aluminium structure. (For interpretation of the references to colour in this figure legend, the reader is referred to the web version of this article.)

then increases to 100 ℃ at a rate of 10 ℃/min, followed by a 2-minute isothermal soaking, and finally cools down to −60 ℃. The preparation and testing procedures of the SE wire are identical to those of the SMA, with the only difference being the weight of the SE sample (7.59 mg) and its corresponding pan (50.39 mg).

3.2. Young's modulus tests

These tests are to investigate the relationship between Young's modulus and temperature, enabling the determination of the shear modulus for the SMA and SE materials. The *strain-controlled dynamic mode* of the DMA Q800 is chosen for these experiments. The temperature is programmed to decrease from 150 ℃ to −40 ℃ at a rate of 1 ℃/min, followed by a 5-minute isothermal soak, and then reheated to 150 ℃ at the same rate. Pre-set parameters in the program include a 5 μm displacement amplitude, 125 % force track and 1 Hz frequency. A 23.63 mm long bare SMA wire is used for the test, while the SE wire measures 25.22 mm in length.

3.3. Shear Stress–strain tests at different temperatures

For understanding the hinge mechanism, we need the mechanical behaviours of the SMA and SE during heating and cooling. Therefore, it is necessary to conduct shear stress–strain experiments to access their torsion performance over a series of temperatures. In this work, for the characterization of the SMA, *the heated state* refers to the temperature when the SMA is fully transformed to the austenite state (here taken as 150 ℃). To obtain SMA's mechanical behaviour during cooling, the temperature range starting from 30 ℃ downwards is selected for the shear stress–strain tests.

SMA 1 is used for tests from 30 ℃ downwards. Prior to the experiments, the specimen is heated to 70 ℃ to guarantee complete recovery of its original shape before each test. Subsequently, it is cooled to the predetermined constant temperatures. During the testing process, the *torsion part* of *SMA 1* is pulled downwards (refer to Fig. 2(b)) at a rate of 300 μm/min until a displacement of 9 mm is achieved. *Displacement-control mode* is employed for the experimental setup to maintain a steadier rotational velocity of the torsion part. The shear stress–strain evaluations for the SMA are executed at temperature intervals spanning from −40 ℃ to 20 ℃ in 10 ℃ increments.

SMA 2 is selected for *the heated state* tests. The *force-control mode* is used to have better control close to the machine's force limit. *SMA 2* is heated to 150 ℃ first and kept at the constant temperature for 3 min. Then, the specimen is subjected to the predetermined force (6–18 N at 3 N interval) at a rate of 1 N/min. Once the pre-set force is reached, the sample is unloaded to 0.01 N at the same rate.

For the SE materials, we do not distinguish between *the heated state* and cooling, as they are expected to show superelastic behaviour, supplying the antagonist force during the whole actuation process of the hinge. The experimental methodology of *SMA 1* is implemented for *SE 1* and *SE 2*, albeit with distinct temperature ranges. *SE 1* undergoes testing from −20 ℃ to 20 ℃, while *SE 2* is subjected to a higher range of 30–50 ℃.

3.4. Superelastic effect tests for SE

To assess the superelastic behaviour, sample *SE 3* is used for a series of displacement-control tests covering a temperature scope from −40 ℃ to 40 ℃ in 10 ℃ intervals. For each constant temperature setting, 4–5 *loading–unloading cycles* are performed on *SE 3* using the *displacement-control method* with several pre-defined target displacements (2.0 mm to 8.0 mm in 2.0 mm increments, and 9.0 mm) at a rate of 300 μm/min. For the temperature below 0 ℃, where the material starts to lose its superelasticity, a heating step to 70 ℃ is incorporated after each loading–unloading cycle to ensure full recovery. Similar tests can be found in chapter 4 of Rao's work [27].

Specific dimensions of nitinol samples used in experiments can be seen in Table 1.

Table 1
Dimensions of the configuration SMA and SE samples used in tests.

Sample	Wire Radius r [mm]	Torsion Length L [mm]	SMA Arm Length La [mm]	SMA Initial Angle θ_0	Aluminium Structure Length Ls [mm]
SMA 1	0.50	12.30	6.60	100°	9.37
SMA 2	0.50	13.24	7.53	148°	6.00
SE 1	0.375	12.77	5.77	111°	8.40
SE 2	0.375	13.35	6.60	140°	8.21
SE 3	0.375	15.91	5.35	113°	9.30

4. Characterisation results

4.1. DSC thermogram for transition temperatures

Fig. 3(a) presents the DSC curves for both SMA and SE, with the black arrows on the thermograms denoting the heating and cooling processes. For the SMA specimen, the heating process from −60 ℃ to 100 ℃ results in an endothermic peak as the SMA transitions from martensite to austenite by absorbing heat energy. Four tangents (indicated by dash-dotted lines in Fig. 3(a)) yield two inflection points: austenite start (A_s^{SMA} = 30.2 ℃) and finish temperature (A_f^{SMA} = 37.8 ℃). During the cooling process, two exothermic peaks can be observed. The first peak at a higher temperature corresponds to the transition from austenite to R-phase, whereas another exothermic peak corresponds to the reaction from R-phase to martensite [28]. Thus, the SMA specimen on cooling exhibits a well-defined two-stage transformation sequence of *austenite-R phase-martensite*. Martensite start (M_s^{SMA}) and finish temperature (M_f^{SMA}) are determined by the exothermic peaks at 16.6 ℃ and −2.5 ℃ correspondingly. As for the SE specimen, represented by the blue curve in Fig. 3 (a), it displays one endothermic and two exothermic peaks. The cooling process of SE is plotted on small scales (see Fig. 3(b)) to define the M_s^{SE} and M_f^{SE}. All transformation temperatures of SMA and SE are listed in Table 2.

Table 2
Transition temperatures of Nitinol wires as determined in the experiments.

Transition Temperatures of Nitinol Wires		SMA	SE
Martensite Start Temperature	M_s	16.6 ℃	0.5 ℃
Martensite Finish Temperature	M_f	−2.5 ℃	−44.8 ℃
Austenite Start Temperature	A_s	30.2 ℃	−18.5 ℃
Austenite Finish Temperature	A_f	37.8 ℃	12.5 ℃

4.2. Young's modulus and shear modulus

Fig. 3 (c) shows the variation of Young's modulus for the SMA and SE during the cooling and heating processes, as determined through dynamic tests at 1 Hz. When the temperature decreases from 150 ℃ to 18 ℃, the Young's modulus of the SMA (red line in Fig. 3 (c)) demonstrates a mild reduction (around 68.2 GPa), followed by a sharp decline to 25.4 GPa at 9.4 ℃, which corresponds to the transformation from the austenite to R phase (refer to Fig. 3(a)). The modulus then increases to 39.0 GPa at −40 ℃. During heating, it produces a gradual decrease to 30.4 GPa at 27.3 ℃ and subsequently experiences a significant increase to 62.3 GPa at 34.9 ℃ due to the *martensite-to-austenite* phase transformation. A reduction in Young's modulus prior to reaching the austenite start temperature during heating (-40 ℃ to 27.3 ℃ in our work) has also been documented in the literature [29,30].

The SE wire has a lower austenite Young's modulus (62.2 GPa at 150 ℃) compared to the SMA (68.2 GPa). This could potentially be attributed to the lower atomic percentage of Ni in the SE alloy [31]. The

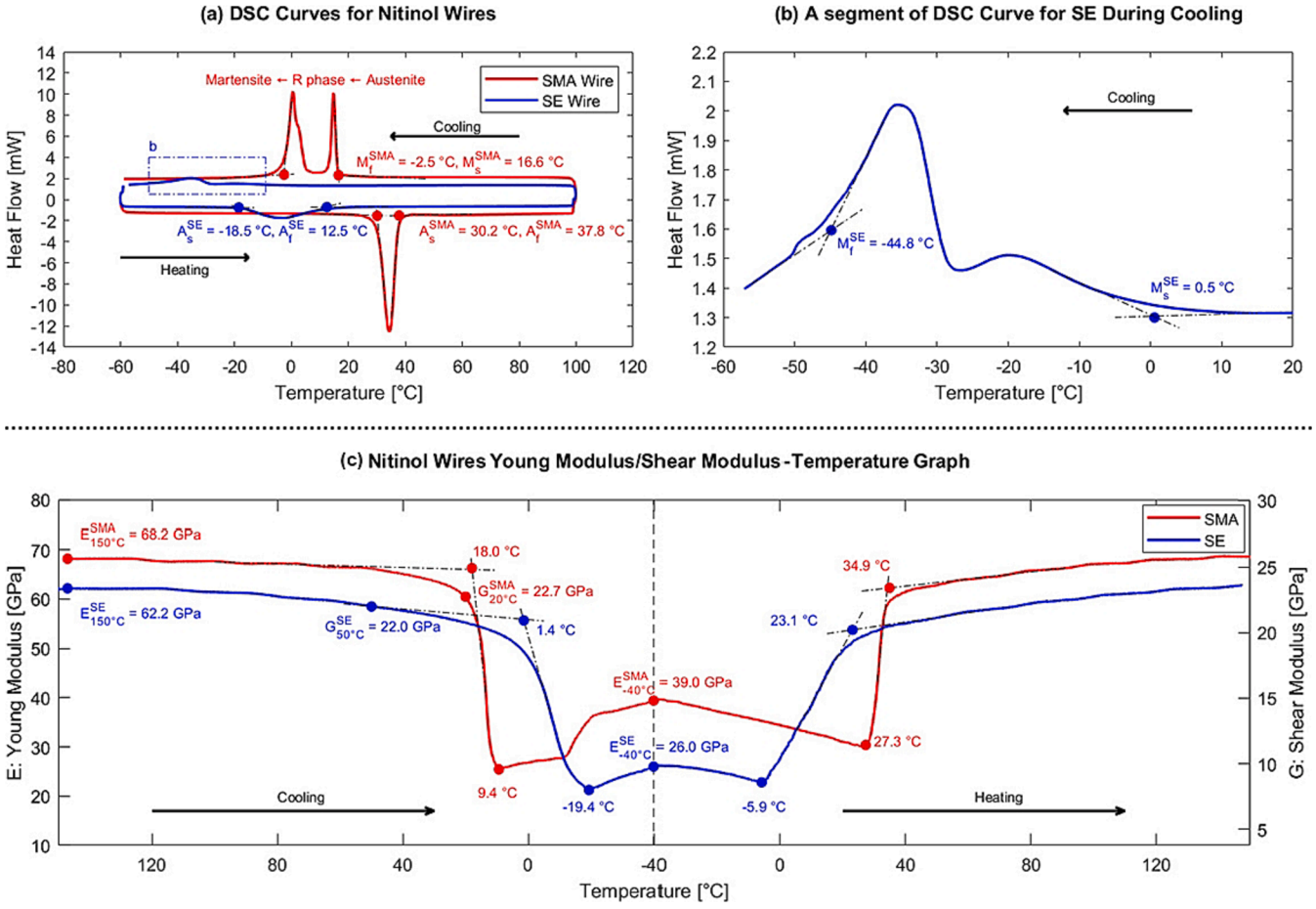

Fig. 3. (a) and (b): DSC thermogram of SMA (red curve) and SE (blue curve). (c): The 1 Hz Young's modulus of the SMA and SE wires as a function of temperature. *E* represents the Young's modulus with scale on the left Y-axis. *G* stands for nitinol's shear modulus on the right Y-axis, which is calculated with the Young's modulus experimental data and the equation $G = E/[2(1 + v)]$. Note that the X-axis follows the time line of the experiment: cooling from 150 ℃ to −40 ℃, followed by heating to 150 ℃. (For interpretation of the references to colour in this figure legend, the reader is referred to the web version of this article.)

cooling process reveals a marked decrease of the modulus, starting at 1.4 ℃, which is close to the martensite start temperatures for SE observed in Fig. 3 (b) (0.5 ℃). During the heating process, between −5.9 ℃ to 23.1 ℃, there is a significant increase in modulus. These temperatures are roughly 10 ℃ higher than the austenite start and finish temperature (-18.5 ℃ and 12.5 ℃) listed in Table 2, which also can be explained by the *stress-induced phase transformation* [29,30].

With the equation $G = E/[2(1 + v)]$, the shear modulus G can be calculated. The Poisson's ratio v, is typically assigned a value of 0.33 in the literature [29,32]. The right Y-axis in Fig. 3(c) is designated as the shear modulus scale. The measured martensite shear modulus of SMA and SE at −40 ℃ are 14.7 GPa and 9.8 GPa respectively, which is within the range of 7.5–15.4 GPa reported in the literature [33,34]. The observed austenite shear modulus values for the SMA and SE at 150 ℃ are 25.4 GPa and 23.4 GPa, which are also close to the 24.8–31.2 GPa documented in [29,34].

4.3. Shear Stress–strain curves at different temperatures

4.3.1. SMA loading during cooling

SMA shear stress–strain curves at different temperatures in the cooling range (from 30 ℃ downwards) are plotted in Fig. 4(a). For the SMA shear stress–strain curve at 20 ℃ (yellow colour), an initial elastic deformation is observed. A black dash-dotted line, representing the SMA martensite shear modulus at 20 ℃ (22.7 GPa derived from Fig. 3(c)), is plotted to compare with the slope of the elastic region (yellow dash-dotted line). The agreement confirms the reliability of the configuration presented in section 2.2 (Fig. 2). In the second region, the deformation transition from twinned to detwinned martensite results in a plateau, during which a minor increase in shear stress induces a substantial increment in shear strain. Following this, as the shear stress increases, the SMA fully transforms into detwinned martensite, and the shear stress–strain curve exhibits a steeper slope. Overall, applying a 150 MPa shear stress on martensite SMA yields an approximate shear strain of 8 %, which is consistent with the findings of Melton *et al.* [30].

When comparing the series of shear stress–strain curves at different temperatures, it is evident that the elastic modulus and martensite stress plateau values decrease with lower temperatures (20 ℃ to −20 ℃), while they increase from −30 ℃ and −40 ℃. This is also consistent with the SMA cooling process depicted in Fig. 3 (c), which shows an increase in modulus during cooling from −20 ℃ to −40 ℃.

4.3.2. SMA loading and unloading at the heated state

SMA shear stress–strain curves at 150 ℃ are depicted in Fig. 4(b). At this temperature, the SMA material is much stiffer as compared to the lower temperature curves of Fig. 4(a) (e.g. 1.2 % shear strain at 150 ℃ versus 12 % at 20 ℃ with 250 MPa) and does not show the characteristic detwinning stress plateaus.

4.3.3. SE loading

SE shear stress–strain curves during loading can be observed in Fig. 4 (c). As the test temperature decreases, the detwinning martensite stress plateau consistently reduces, while the shear modulus (slope during the first 1 % strain) displays a notable decrease at −20 ℃, which aligns with the low SE shear modulus value at −19.4 ℃ observed in Fig. 3(c). The SE shear modulus at 50 ℃, acquired from the dynamic test, is added for comparison (black dash-dotted line in Fig. 4(c)). Good correspondence can be observed between the quasi-static tests of Fig. 4(c) and the dynamic test of Fig. 3(c) for the measurements at 50 ℃.

4.4. Superelastic behaviour of SE

The outcomes of the loading–unloading experiments for the superelastic material are presented in Fig. 5, where subfigures 5(a)-(d) reveal the performance of *SE 3* for temperatures above 10 ℃. It can be observed that *SE 3* can fully recover to its original shape even after applying a strain up to 8 %. For lower temperatures, significant residual strains start to build up and the material begins to exhibit diminished superelastic properties. Larger applied shear stress results in increased residual strains. For instance, a 9 mm displacement alteration of *SE 3* at −10 ℃ induces 5.5 % residual strain, whereas a 4 mm displacement alteration yields a 1.5 % residual strain (Fig. 5(f)). The test results from −20 ℃ to −40 ℃ can be seen in section S5 of the supplementary information.

5. Modelling

With the experimental data obtained in section 4, we now have enough information to set up a model to describe the *minimum and maximum actuation angles* (θ_{min} and θ_{max}) of a hinge structure (Fig. 1). In this section we will develop a phenomenological model which can directly relate the chosen geometrical parameters (wire diameters and torsion lengths, initial pre-trained angles) and material properties (modulus and its relationship with temperature) to predictions of the θ_{min} and $\theta_{max}$of the hinge actuator.

Our aim is to develop a practical model which can be used by other scientists, engineers and designers to understand and optimize the mechanical behaviour of objects with the hinge structures proposed in this paper. Because of that, we choose to simplify the constitutive behaviour (i.e. the loading and unloading curves) as much as possible without losing too much in the accuracy of the deformation predictions. Note that in general, the *shape of the deformation curves* of other nitinol SMA

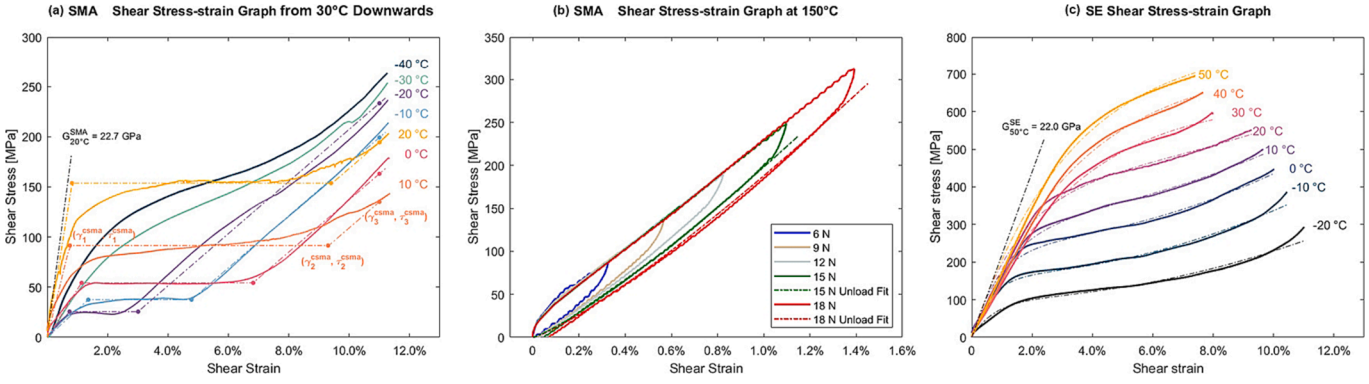

Fig. 4. (a) SMA shear stress–strain curves from 30 ℃ downwards. The coloured dash-dotted lines and connection points ($\gamma_i^{cSMA}, \tau_i^{cSMA}$) are used for modelling in section 5.2.1. (b) SMA shear stress–strain curves at the heated state (150 ℃). The coloured dash-dotted curves are also used for modelling in section 5.2.2. (c) SE shear stress–strain loading curves at different temperatures. The coloured dash-dotted curves are used for modelling in section 5.3.1. The dash-dotted black line corresponds to the shear modulus obtained from the dynamic measurements of Fig. 3(c).

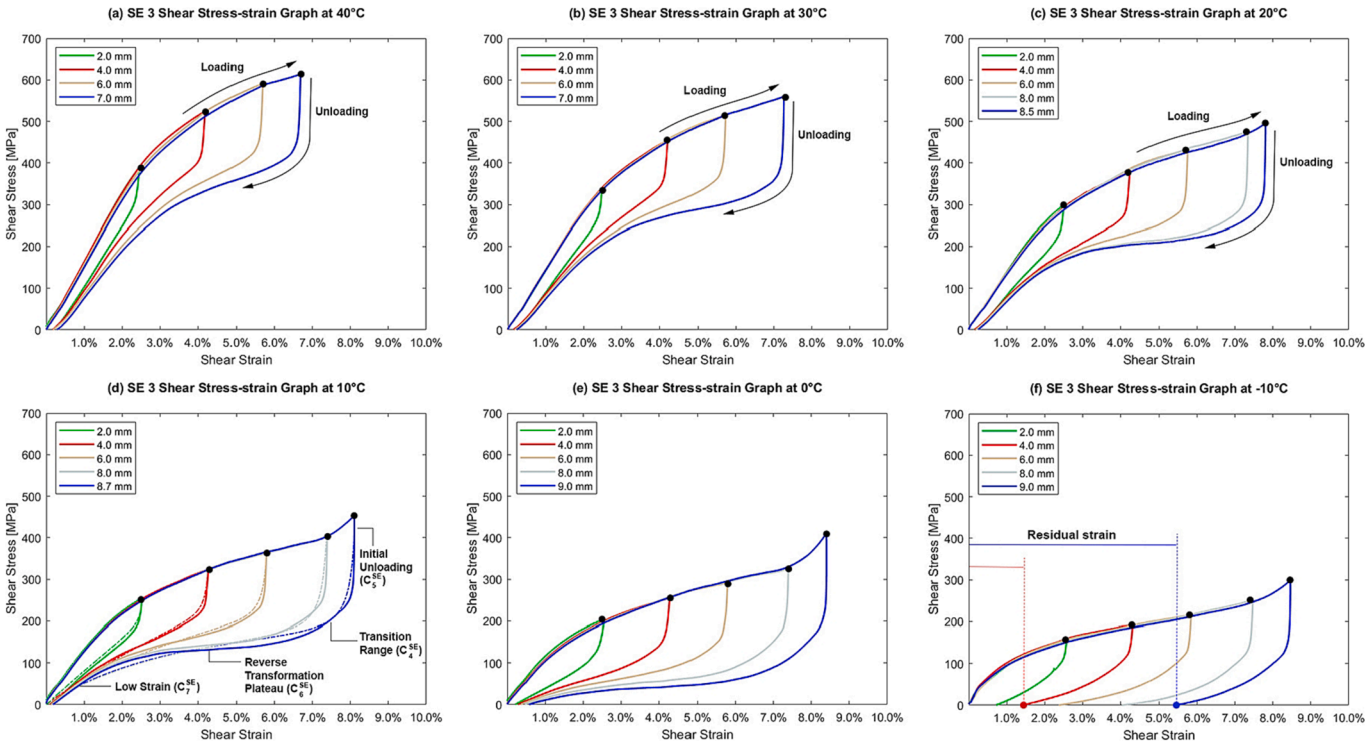

Fig. 5. Superelastic tests in different temperatures. For each experiment, 4–5 loading–unloading cycles are conducted with the displacement-control method. Subgraphs (a)-(c) indicate the SE loading and unloading process with arrows. In subgraph (d), the coloured dash-dotted curves are the fits (for the unloading curves) established in section 5.3.2. Every unloading curve is divided into four segments: initial unloading part, transition range, reverse transformation plateau and low strain. Each segment of the unloading curve has a coefficient (corresponding to Eq. (9) which affects its shape.

and SE materials will be very similar to the materials used in this study and mainly differ in the transition temperatures, which means that the model below remain valid and only the parameter values need to be adapted.

5.1. Reversible torsion hinge analysis

The actuation span of our proposed hinge system in Fig. 1 simply follows from a balance between the torque exerted by the SMA wire (which tries to open the hinge) and that of the SE (which closes the hinge):

$$\mathrm{T}^{SMA}\left(\theta_0^{SMA}, L^{SMA}, r^{SMA}\right) = \mathrm{T}^{SE}\left(\theta_0^{SE}, L^{SE}, r^{SE}\right) \tag{1}$$

where T is the torque of SMA or SE, and it is related to the initial pre-trained angle θ_0, torsion length L and the nitinol wire radius r.

What makes the analysis more complex is that both materials have an intrinsic mechanical hysteresis (difference between the loading and unloading curves, see Fig. 5). When the hinge structure is assembled, the SMA wire, which is initially at 180°, is loaded *anticlockwise* whereas the SE wire is deformed *clockwise* (see Fig. 1). The initial angle of the hinge structure is thus found from the equilibrium of the *two loading curves*. When heated in the first actuation cycle, the SMA tends to move back towards its pre-trained initial angle (180°), while the SE wire further deforms to a larger opening angle. That is, during the first (and subsequent) heating cycles, *the SMA is unloading and the SE is loading*. When cooling down, the SMA modulus drops and the SE starts to close the hinge, i.e., *during cooling the SMA is in loading and the SE is in unloading mode*.

In the subsequent sections, we will set up approximate phenomenological models describing the loading and unloading behaviour of both the SMA and SE materials.

5.2. Modelling of SMA shear Stress–strain curve

5.2.1. SMA loading during cooling

The loading is characterised by a large shear stress plateau in which further stretching induces a phase transformation (from twinned to detwinned martensite [27]). Such transformation only requires a minimum of deformation energy (see Fig. 4(a)). In order to capture the essentials of the deformation curves, we choose to approximate the data in Fig. 4(a) with a curve consisting of three connected linear segments. The first segment represents the elastic deformation of the SMA in its twinned martensite state, the second part describes the material response during detwinning, which is assumed to be horizontal in our work. The third segment is the further loading in the fully detwinned state.

For every temperature, three *connection points* denoted as $\left(\gamma_i^{cSMA}, \tau_i^{cSMA}\right)(i = 1, 2, 3)$ between the different segments are used to formulate the model:

$$\tau^{cSMA}(\gamma) = \begin{cases} \left(\dfrac{\tau_1^{cSMA}}{\gamma_1^{cSMA}}\right)\gamma 0 \le \gamma < \gamma_1^{cSMA} \\ \tau_2^{cSMA}\gamma_1^{cSMA} \le \gamma < \gamma_2^{cSMA} \\ \left(\dfrac{\tau_3^{cSMA} - \tau_2^{cSMA}}{\gamma_3^{cSMA} - \gamma_2^{cSMA}}\right)\left(\gamma - \gamma_3^{cSMA}\right) + \tau_3^{cSMA}\gamma_2^{cSMA} \le \gamma < \gamma_3^{cSMA} \end{cases} \tag{2}$$

We use MATLAB software to first determine the *connection points* $\left(\gamma_i^{cSMA}, \tau_i^{cSMA}\right)$ for loading curves from −20 ℃ to 20 ℃ separately (dash-dotted lines in Fig. 4(a)). γ_3^{cSMA} is assigned a same value of 11.5 % for all temperatures. To determine the temperature dependency of shear strain, we plot (T, γ_i^{cSMA}) $(i = 1, 2)$ as blue triangles and round dots in Fig. 6(a). Similarly, (T, τ_i^{cSMA}) are plotted in red colour. As the detwinning plateau is assumed to be horizontal, τ_1^{cSMA} and τ_2^{cSMA} have a same value for each temperature and both of them are presented as red round dots. MATLAB is used to experiment with various models for fitting data points shown in Fig. 6(a). The *coefficient of determination* (R^2) is referred to for

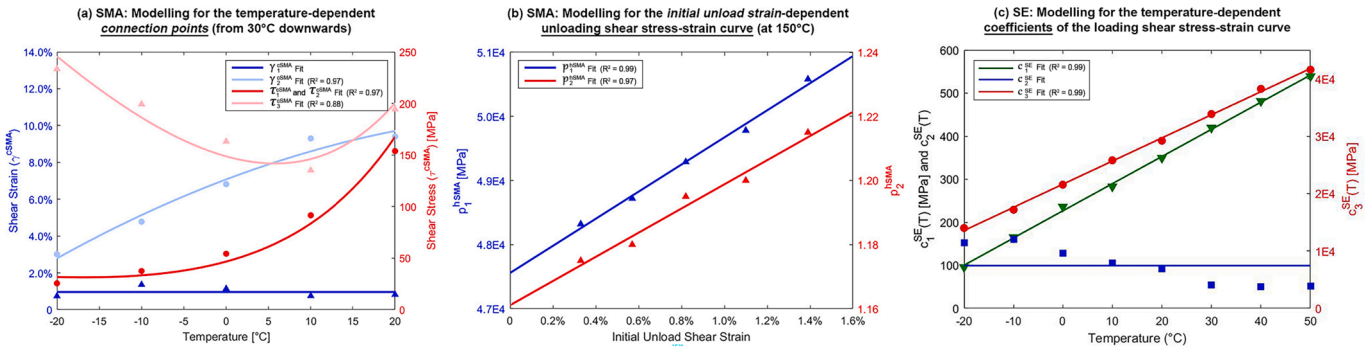

Fig. 6. (a) Modelling for the temperature-dependent connection points (from 30 °C downwards). The data points correspond to $(\gamma_i^{cSMA}, \tau_i^{cSMA})$ of the fitting functions in Fig. 4(a) of the manuscript. The full lines are the fitting models (Eqs. (3) and (4). (b) Modelling for the initial unload strain-dependent of the unloading shear stress–strain curve (at 150 °C). The data points are the fitting parameters (Eq. (5) of the SMA unloading model (dash-dotted lines in Fig. 4(b)). The full lines are the models which characterize the relationship between p_1^{hSMA}, p_2^{hSMA} and the initial unload shear strain (Eq. (6). (c) Modelling for the temperature-dependent coefficients of the SE loading shear stress–strain curve. To simplify, c_2^{SE} is modelled as a constant. The data points correspond to the fitting parameters of the coloured dash-dotted lines in Fig. 4(c). The full lines are the fitting functions of the data points.

evaluating and deciding which model to use. Finally, the temperature dependency of the shear strain is modelled as a second-order polynomial, while for the shear stress, a combination of a linear and exponential term is used (Eqs. (3) and (4). The fit parameters and its error bounds are determined by MATLAB and listed in Table 3.

$$\gamma_i^{cSMA}(T) = p_{1_i}^{cSMA}T^2 + p_{2_i}^{cSMA}T + p_{3_i}^{cSMA}(i = 1,2,3) \tag{3}$$

$$\tau_i^{cSMA}(T) = p_{4_i}^{cSMA}e^{p_{5_i}^{cSMA}T} + p_{6_i}^{cSMA}T(i = 1,2,3) \tag{4}$$

where $(\gamma_i^{cSMA}, \tau_i^{cSMA})$ are the the *connection points* of SMA shear-strain curves, T is the temperature.

With the Eqs.2–4 and parameters in Table 3, we can model the SMA loading curves at any temperature from 30 °C downwards.

5.2.2. SMA unloading at the heated state

As explained in section 5.1, during the heating cycles of the hinge system, *the SMA is unloading and the SE is loading*. Therefore, for SMA, we only model the unloading curve at high temperature. The shear stress–strain curves at 150 °C in Fig. 4(b) are used for modelling. Although the curves are nearly linear, for accurate prediction of the *maximum actuation angle*, it turns out to be necessary to use a power function (Eq. (5) to fit the unloading curves (see dash-dotted lines in Fig. 4(b)).

$$\tau^{hSMA}(\gamma) = p_1^{hSMA}\gamma^{p_2^{hSMA}} \tag{5}$$

It can be seen that the SMA unloading curves at 150 °C are different owing to the distinct *initial unload shear strain*, which means the coefficients p_1^{hSMA} and p_2^{hSMA} are different among these curves. To evaluate how the *initial unload shear strain* affects p_1^{hSMA} and p_2^{hSMA}, we plot $(\gamma_{unload}^{hSMA}, p_1^{hSMA})$ and $(\gamma_{unload}^{hSMA}, p_2^{hSMA})$ with blue and red triangles accordingly (see Fig. 6(b)). It can be seen that p_1^{hSMA} and p_2^{hSMA} vary linearly with the *initial unload shear strain* γ_{unload}^{hSMA}:

$$p_i^{hSMA}(\gamma_{unload}^{hSMA}) = q_{i_1}^{hSMA}\gamma_{unload}^{hSMA} + q_{i_2}^{hSMA}(i = 1,2) \tag{6}$$

in which q_{i1}^{hSMA} and q_{i2}^{hSMA} $(i = 1,2)$ are two parameters to define p_i^{hSMA}. Their values are provided in Table 3.

5.3. Modelling of SE shear Stress–strain curve

5.3.1. SE loading

The SE shear stress–strain curves during loading are showed in Fig. 4 (c) and can be approximated as:

$$\tau^{SE}(\gamma) = c_1^{SE}\left[1 - \exp\left(-c_2^{SE}\gamma\right)\right] + c_3^{SE}\gamma^2 \tag{7}$$

in which the coefficient c_1^{SE} is a measure of the shear stress level of the detwinning plateau, c_2^{SE} determines the slope of the initial elastic part (shear modulus), c_3^{SE} affects the increase rate of shear stress after the detwinning deformation.

To figure out the effect of temperature on c_1^{SE}, c_2^{SE} and c_3^{SE}, we plot $(T, c_i^{SE})(i = 1,2,3)$ with green triangles, blue squares and red round dots respectively in Fig. 6(c). It can be seen that they can be approximated with a linear model:

$$c_i^{SE}(T) = p_{1_i}^{SE}T + p_{2_i}^{SE}(i = 1,2,3) \tag{8}$$

5.3.2. SE unloading

The unloading curves of the SE material are needed to describe the closing process of the hinge deformation. Fig. 5 shows that the SE unloading curves depend on the temperature and the *initial unload shear strain*. All subgraphs show a large similarity in shapes. To illustrate this, we combined the unloading curves of 10–30 °C in a single plot. As can be observed from Fig. 7(a) and (b), a vertical shift with factor α relative to

Table 3
Parameters for the SMA model.

Parameters					
$p_{1_1}^{cSMA}$ [%/c2]	0	$p_{1_3}^{cSMA}$ [%/c2]	0	$p_{4_3}^{cSMA}$ [MPa]	143 (±32)
$p_{2_1}^{cSMA}$ [%/c]	0	$p_{2_3}^{cSMA}$ [%/C]	0	$p_{5_3}^{cSMA}$	0.05 (±0.010)
$p_{3_1}^{cSMA}$ [%]	0.96 (±0.343)	$p_{3_3}^{cSMA}$ [%]	11.5	$p_{6_3}^{cSMA}$ [MPa]	−10 (±2.9)
$p_{1_2}^{cSMA}$ [%/c2]	-2×10^{-3} ($\pm 7.4 \times 10^{-3}$)	$p_{4_1}^{cSMA}$ [MPa]	47 (±16)	$q_{1_1}^{hSMA}$ [MPa]	2×10^5 ($\pm 0.3 \times 10^5$)
$p_{2_2}^{cSMA}$ [%/c]	0.17 (±0.088)	$p_{5_1}^{cSMA}$	0.07 (±0.013)	$q_{1_2}^{hSMA}$ [MPa]	5×10^4 (±310)
$p_{3_2}^{cSMA}$ [%]	7.1 (±1.93)	$p_{6_1}^{cSMA}$ [MPa]	−1.0 (±1.47)	$q_{2_1}^{hSMA}$	3.7 (±1.13)
				$q_{2_2}^{hSMA}$	1.2 (±0.01)

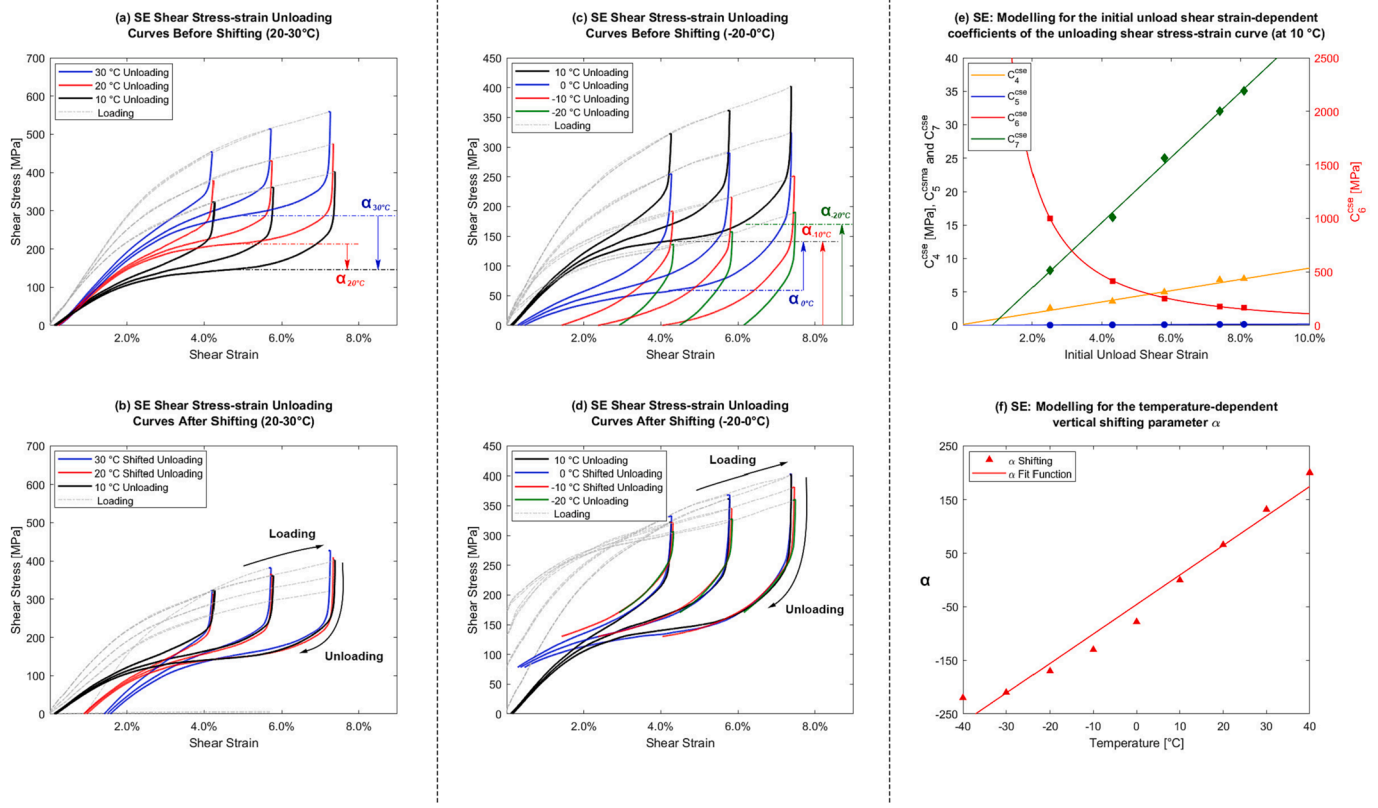

Fig. 7. (a)-(d): SE unloading curves at other temperatures overlap with the curves at 10 °C after vertical shifting. (e): Modelling for the initial unload shear strain-dependent coefficients (at 10 °C). The data points are the fitting parameters of the coloured dash-dotted curves in Fig. 5(d), which corresponds to Eq. (9). Full lines characterize their relationships with the initial unload shear strain. (f): Modelling for the temperature-dependent vertical shifting parameter α.

Table 4
Parameters for SE loading and unloading model.

Parameters					
$p_{1_1}^{SE}$ [MPa/c]	6.3 (±0.45)	$p_{1_2}^{SE}$	0	$p_{1_3}^{SE}$ [MPa/C]	403 (±30)
$p_{2_1}^{SE}$ [MPa]	226 (±1)	$p_{2_2}^{SE}$	99 (±3)	$p_{2_3}^{SE}$ [MPa]	2×10^4 (±29)
$p_{1_4}^{SE}$ [MPa]	84 (±12)	$p_{1_5}^{SE}$	2.0 (±0.02)	$p_{1_6}^{SE}$ [MPa]	2.7 (±0.90)
$p_{2_4}^{SE}$ [MPa]	0.15 (±0.719)	$p_{2_5}^{SE}$	7×10^{-4} ($\pm 14.0 \times 10^{-4}$)	$p_{2_6}^{SE}$	−1.6 (±0.09)
$p_{1_7}^{SE}$	486 (±46)	q_1^{SE} [MPa/c]	5.5 (±0.82)		
$p_{2_7}^{SE}$	4.1 (±10.91)	q_2^{SE} [MPa]	−45 (±21.3)		

the 10 °C curve indeed results in a good overlap. Therefore, we now only need to model the shape of 10 °C reference curve, to be able to predict the unloading behaviour at higher temperatures using the factors α. For a good prediction of the hinge angles, it turns out that we require a detailed description of the initial part of the SE unloading curve (i.e. the steep declining of *the initial unloading part* as well as *the transition range*, see Fig. 5(d)). For this, we propose to use a tan function (first part of Eq. (9). The second part of Eq. (9) describes the shear stress–strain behaviour near the origin. The fitting results are shown as coloured dash-dotted curves in Fig. 5(d).

$$\tau_{unload}^{SE}(\gamma_{unload}^{SE}) = c_4^{SE}\tan\left(\frac{\pi\gamma_{unload}^{SE}}{c_5^{SE}}\right) + c_6^{SE}\left[1 - \exp\left(-c_7^{SE}\gamma_{unload}^{SE}\right)\right] \tag{9}$$

where γ_{unload}^{SE} is SE shear strain of the unloading phase, τ_{unload}^{SE} is the SE shear stress as a function of shear strain at 10 °C, c_4^{SE}, c_5^{SE}, c_6^{SE} and c_7^{SE} are coefficients of the model. c_4^{SE} determines the *transition range* (see Fig. 5 (d)). c_5^{SE} relates to the *initial unloading part*. c_6^{SE} affects the shear stress level of the *reverse transformation plateau*, while c_7^{SE} has influence on the slope of *low strain part* before recover to 0.

A Similar shifting can be done for the temperatures below 10 °C, as shown in Fig. 6(c) and (d). Note that with vertical shifting the *low strain part* is not captured well, however, as mentioned before, we only need a detailed description of the initial unloading behaviour.

For a given temperature (10 °C), the unloading curves differ from each other owing to the distinct *initial unload shear strain*. To model this, we plot the coefficients c_4^{SE}, c_5^{SE} and c_7^{SE} as a function of the initial shear strain γ_{unload}^{SE} (see Fig. 7(e)), and model these as linear functions:

$$c_j^{SE}(\gamma_{unload}^{SE}) = p_{1_j}^{SE}\gamma_{unload}^{SE} + p_{2_j}^{SE}(j = 4, 5, 7) \tag{10}$$

The coefficient c_6^{SE} is modelled as:

$$c_6^{SE}(\gamma_{unload}^{SE}) = p_{1_6}^{SE}\left(\gamma_{unload}^{SE}\right)^{-p_{2_6}^{SE}} \tag{11}$$

In addition, the vertical shifts α are plotted as a function of temperature and also fitted to a linear model (full line in Fig. 7(f)):

$$\alpha(T) = q_1^{cSE}T + q_2^{cSE} \tag{12}$$

With the Eqs. 7–12 as well as the Table 4, we can obtain the SE loading and unloading curve with given *initial unload shear strain* and temperature.

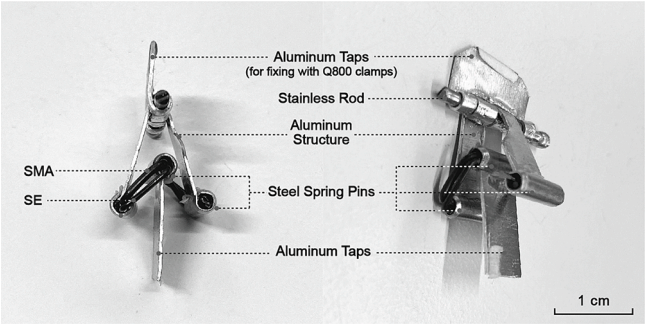

Fig. 8. Configuration of the reversible torsion hinge system for validation tests in the Q800.

6. Model validation

In order to validate our hinge angle prediction model (Eqs. 1–12), we construct five different hinge structures, which differ in the lengths of the torsion element as well as in the initial deformation angles. These hinges are subjected to heating and cooling cycles and the corresponding angle changes are monitored. Using the models proposed in section 5, we then predict how the angle changes vary with temperature and compare this with our measurements.

6.1. Experiments with 5 reversible hinges

The validation tests of an opening and closing hinge structure could in principle be done by placing the hinge in an oven and using a camera system to infer the hinge angle changes during heating and cooling. In order to have a more accurate control of temperature and hinge deformation however, we prefer to do these tests in the DMA Q800 with a tool as shown in Fig. 8. The hinge system is integrated with a SMA and SE using three galvanized steel spring pins. During the testing, only a small force (0.01 N) is applied and the testing machine essentially follows the movements of the hinge system. Eqs. (S1)-(S4) and (S8) in supplementary information are used to calculate the opening angle from the detected displacement.

Five tests are conducted with different hinge systems (labelled as *Sys 1–5* in Table 5) to examine the effect of SMA pre-trained initial angle and torsion length variation on the system angle change. The SEs of *Sys 1–5* are identically configured and trained in terms of initial angle (0°) and torsion length (10.45 ± 0.25 mm). SMA with varying initial pre-trained angles but an equal torsion length (11.0 ± 0.4 mm) is used for *Sys 1–3*. Conversely, *Sys 3–5* consist of SMAs with different torsion lengths but an equal initial angle (270°).

Prior to the test, the temperature is decreased to −40 ℃ and maintained constant for 5 min. Subsequently, the temperature is increased to 150 ℃ at a rate of 5 ℃/min, followed by another 5-minute isothermal soaking. Then, the system is cooled down to −40 ℃ at the same rate. The heating–cooling cycle is performed twice. The second recorded displacement variation of five systems is converted to the actuation angle of the hinge system, which is plotted versus temperature in Fig. 9 (*Sys 1–3* in (a), *Sys 4* and *Sys 5* in (b) and (c) respectively).

As shown in Fig. 9(b), during the heating process, the hinge angle of *Sys 4* (green curves) remains constant for a large part at 90° (*minimum actuation angle*), and only changes in a narrow temperature range from 46 ℃ to 92 ℃ during the SMA's phase transition. When the torque produced by SMA balances with SE's, the system angle becomes stabilize after 92 ℃. For the cooling process, the system angle starts to reduce at around 20 ℃. It completely recovers to 90° at −16 ℃. Similar results can also be observed with other specimens (see Fig. 9(a) and (c)). For definitions of the *minimum and maximum actuation angle*, as well as the *angle span* refer to Fig. 1.

6.2. Model predictions

To better understand how the torques of the SMA and SE wires interact during the different parts of the cooling curves, we identify three states: *the heated state, locked state,* and *actuation state*. *The heated state*, denoted by the symbol in Fig. 9(c), describes the condition where the system is held at its highest temperature (150 ℃). During the first and the last parts of the cooling (and as shown in Fig. 9(c)), the hinge system angle remains constant, which will be referred to as *the locked state*. *The actuation state*, represented by the part, refers to the temperature range in which the hinge angle changes. Our objective is to investigate how the SMA and SE behaviour determine the hinge angle of the system in each of these states.

6.2.1. The heated state

As stated in section 5.1, the heating actuation process corresponds to the *loading phase of the SE and unloading phase of SMA*. In order to visualize the torque equilibrium between SMA and SE wires (Eq. (1), we plot the unloading curves of SMA in Fig. 10(a) and (b), together with the loading curves of the corresponding SE wires. The intersections indicate that the torques of the SE and SMA wire (from the same system) balance out, resulting in 5 predictions for the *maximum actuation angles* (all at 150 ℃) [23]. The relationship between shear strain and shear stress is given by Eqs. 1–12. Additionally, to achieve the angle-torque graphs, another three equations are required.

$$T = \frac{\tau J}{r} \tag{13}$$

$$\theta = \frac{\gamma L}{r} \tag{14}$$

$$J = \frac{\pi r^4}{2} \tag{15}$$

where T is the torque, J is the polar moment of inertia of SMA or SE, r is the radius of SMA or SE, L is the length of *torsion part* (see Fig. 2).

Fig. 10(a) and (b) illustrates *the heated state* of *Sys 1–5*. As listed in Table 5, *Sys 1–5* share the same initial angle of 0° and have similar torsion lengths for the SE. Consequently, their angle-torque curves almost overlap in the graph (black curves in Fig. 10(a) and (b)). *Sys 1–3* have different SMA initial pre-trained angles (see black arrows in Fig. 10 (a)), resulting in different starting angles. The deformation curves however have identical shapes. The equilibrium angles for *Sys 1–3* follow from the intersection points are determined as 58°, 101° and 154°, respectively. The effect of the torsion length for systems with constant SMA initial angles of 270° is shown in Fig. 10 (b). In this case,

Table 5
Geometric parameters of hinge systems. Definitions of parameters refer to Fig. 2.

Hinge System	Initial Angle θ_o	Torsion Length L [mm]	Arm Length La [mm]	Aluminium Structure Length Ls [mm]
Sys 1	**SMA 104°** + SE 0°	SMA 10.6 mm + SE 10.2 mm	7.3 mm	13.9 mm
Sys 2	**SMA 175°** + SE 0°	SMA 11.1 mm + SE 10.7 mm	7.2 mm	13.8 mm
Sys 3	**SMA 270°** + SE 0°	**SMA 11.3 mm** + SE 10.3 mm	7.3 mm	13.1 mm
Sys 4	SMA 270° + SE 0°	**SMA 13.4 mm** + SE 10.2 mm	7.3 mm	13.1 mm
Sys 5	SMA 270° + SE 0°	**SMA 17.6 mm** + SE 10.2 mm	7.5 mm	13.4 mm

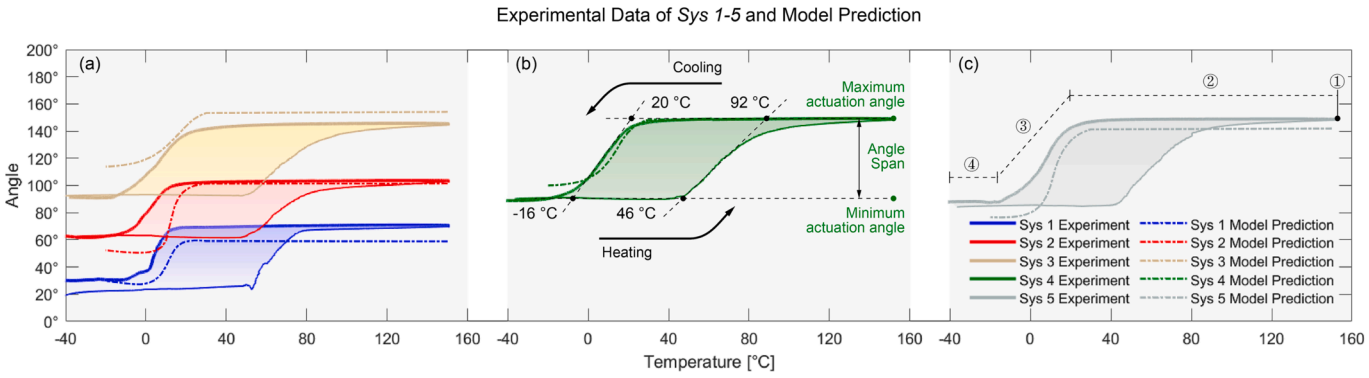

Fig. 9. Experimental results of 5 reversible torsion hinges: Sys 1–3 are plotted in (a), while Sys 4 and Sys 5 are in (b) and (c) respectively. The full lines are the experimental data, whereas the coloured dash-dotted lines are the prediction model of the cooling process. The shaded areas reflect the hysteresis. Minimum and maximum actuation angle, as well as the angle span correspond to Fig. 1. The cooling curve in (c) is divided into 4 parts (, and), of which more details are discussed in section 6.2.

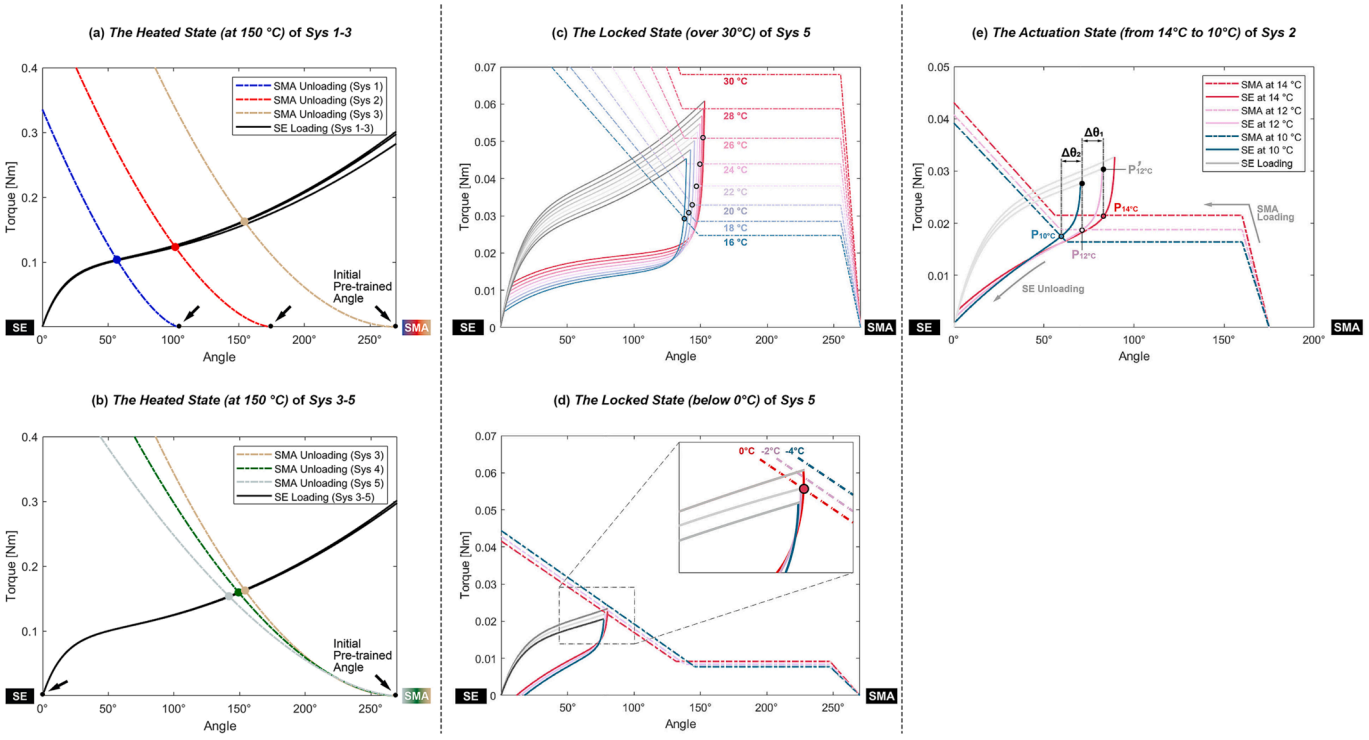

Fig. 10. (a) and (b): *The heated state* of *Sys 1–3* and *Sys 3–5* at 150 °C. The initial pre-trained angles of the nitinol wires are shown as black arrows. The coloured dots represent the intersections between the SMA unloading and the SE loading torques. (c) and (d): Explanation of *the locked state* for *Sys 5*. The coloured full lines represent the SE unloading at different temperatures, while grey lines are the SE loading curves. Coloured dash-dotted lines represent the SMA loading curves. There is no intersection between the torque–angle curves when the temperature is above 30 °C or below 0 °C. (e): *The actuation state* of *Sys 2* from 14 °C to 10 °C. $\Delta\theta_1$ and $\Delta\theta_2$ are the angle change of two cooling steps (from 14 °C to 12 °C, and 12 °C to 10 °C).

the intersection points turn out to be 142°, 149° and 154°, which are seen to vary much less.

6.2.2. Locked state

During the first part of cooling, the hinge angle remains locked at *the heated state* angle in Fig. 9(c)). The reason for this can be explained by the details of SMA and SE mechanical behaviour. As illustrated in Fig. 10 (c), when cooling toward 30 °C, the SMA wire is in its torque plateau region, which is above the torque generated by the SE material. This indicates that the SE, within the system, is incapable of producing and transferring sufficient torque to move the SMA. During further cooling of the system, the SMA torque plateau decreases (to about 0.06 Nm at 28 °C) until the unloading torque of the SE surpasses that of the SMA and *the actuation state* starts.

After the actuation, a second *locked state* can be observed (in Fig. 9 (c)). As can be seen in Fig. 10(d), this happens below 0 °C, where the SE torque drops below the torque generated by the SMA.

6.2.3. Actuation state

During the cooling, the equilibrium hinge angles at *the actuation state* can be analyzed in a similar way. In Fig. 10(e), we use *Sys 2* as an example. At 14 °C, the SMA balances with SE at 84° P14C in Fig. 10(e)). When the temperature is decreased to 12 °C and 10 °C, the intersection points shift to 71° (pointP12C) and 59° (pointP10C) respectively. Note that the angle change is relatively large for only a small temperature variation.

6.3. Comparison of experimental data with the hinge model

With the analysis method mentioned in section 6.2, the angle-temperature curve of the system's cooling process can be modelled. Fig. 9 presents the experimental data of the cooling process (coloured full lines) as well as the corresponding model predictions (coloured dash-dotted lines). The *angle span* of all five specimens closely matches the model's predictions, yielding an average deviation of 17.7 % (mainly due to vertical shifts). The deviations between the predicted and experimental *maximum and minimum actuation angle* are 10.6 % and 16.0 % correspondingly. The overall deviation is 13.5 ± 8.2 %.

Going from *Sys 1–3*, Fig. 9(a) shows that the predictions for the *maximum actuation angle* deviate from the observation by −12°, −2° and + 9°, respectively. The *minimum actuation angles* are overpredicted by −3°, −11° and + 23° correspondingly. Their *actuation states* (angles decrease) start earlier by about 10 ℃. For *Sys 4*, the *maximum actuation angle*, as well as *the actuation state* (from 20 ℃ to −16 ℃) is predicted well (Fig. 9(b)) and only the *minimum actuation angle* is somewhat overpredicted (+8°). The predicted *angle span* of *Sys 5* aligns well with the experimental data, which only has 4° deviation, while both the *maximum and minimum actuation angle* are overpredicted by around 8°.

7. Discussion and application examples

The experiments with the five constructed hinges show that during most of the heating and cooling process the hinge angle does not change and that the actuation of the structure is limited to a relatively narrow temperature window. Interesting to see is that these temperature windows differ from the transition ranges of the SMA material as determined with DSC (see Fig. 3(a) and Table 2). As is discussed in section 6, this is explained with the fact that the hinge actuation depends on details of the mechanical behaviour of both the SE and SMA material. More details about the actuation temperature of the hinge system can be seen in the supplementary information. Our model which takes these details into account was seen to predict the actuation transitions of the hinge mechanism quite accurately.

7.1. SMAs' geometric parameters influence on system angles

The two main parameters for the design of the hinge actuator are the SMA pre-trained initial angle and the torsion length. In Fig. 11(a), we plot the *maximum and minimum actuation angle* (θ_{max} and θ_{min}), as well as the *angle span* ($\Delta\theta$) for different SMA pre-trained angles. As can be seen, the *maximum actuation angle* (dash-dotted line) increases linearly with the SMA pre-trained angle, but this is not the case for the *minimum actuation angle* (dotted line), which starts to increase only for the pre-trained angle above 170°. Because of this, increasing the SMA pre-trained angle does not automatically lead to larger an actuation span, which actually shows a maximum of about 40° for a pre-trained angle of 170° (see the full line). The coloured symbols in Fig. 11 refer to the results of the validation experiments (obtained from Fig. 9) and are shown to closely follow the predictions.

Fig. 11(b) shows the effect of SMA torsion length on the system angles. Upon increasing the SMA torsion length, the *maximum actuation angle* shows a gentle decrease, while the *minimum actuation angle* declines faster, thereby leading to a growth in the actuation span. The *angle span* increases with the torsion length from 40° at 1 cm to 80° at 2 cm torsion length. The largest experimentally observed *angle span* is about 60°.

Overall, a greater SMA preset angle results in a larger *maximum and minimum actuation angle*, while a longer torsion length induce a larger *angle span*.

7.2. Applications

Reversible torsion hinge actuators are lightweight, and have a small form factor while delivering high actuation force. *Sys 5* only weighs 2 g, but can produce up to 5 N actuation force when heated at high temperature (see supplementary information). These attributes render them a competitive alternative to motors or other forms of actuators in some application scenarios. For instance, a gripper constructed by these hinge actuators can securely grasp objects of various shapes and sizes (Fig. 12 (a) and (b)) without inflicting damage, whereas a motor-based gripper may require the integration of force-feedback sensors to prevent harm caused by excessive force. A butterfly demonstrator is represented as another example in Fig. 12(c). Furthermore, these millimeter-scale hinge actuators have promising prospects applications with spatial constraints, such as aerospace and medical surgical instruments. The reversible torsion hinge actuator can be activated by electrical current within a few seconds. However, cooling down naturally in room temperature air requires much more time (30–40 s). It means that the actuator is not very suitable for applications which need high response speed, such as a robot hand with fast moving fingers, and real-time responsive VR devices. To reduce the cooling time, airflow speed can be increased, and thinner SMA wires can be used to developed the hinge actuators. The hinge actuator can also be activated in water, requiring about 3 to 5 s for both heating and cooling.

8. Conclusion

This paper discusses a novel reversible hinge actuator composed of a nitinol shape memory alloy wire and a superelastic wire which are actuated in torsion. We measured and modelled the mechanical properties of these materials in detail, for which we constructed a special loading frame to convert tension to torsion deformation. The actuation behaviour of the hinge opening follows from the equilibrium between the loaded SMA and SE wires, resulting in an overall model for the hinge behaviour. We constructed 5 reversible hinge systems with different SMA pre-trained angles and torsion lengths, and used these to validate our model. The *angle span* seems to increase with SMA torsion length up

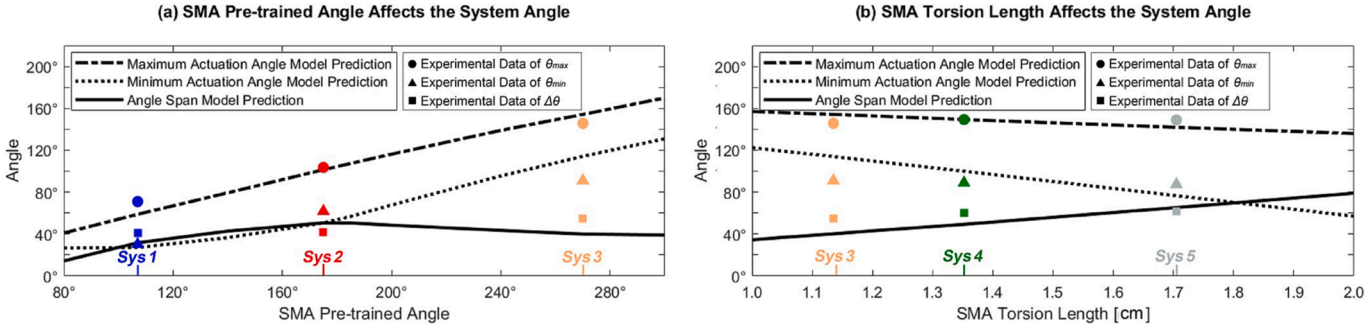

Fig. 11. (a) Influence of the SMA pre-trained angle on the system angles. (b) Effects of the SMA torsion length on the system angles. Lines indicate model predictions, and symbols are the independent experimental data.

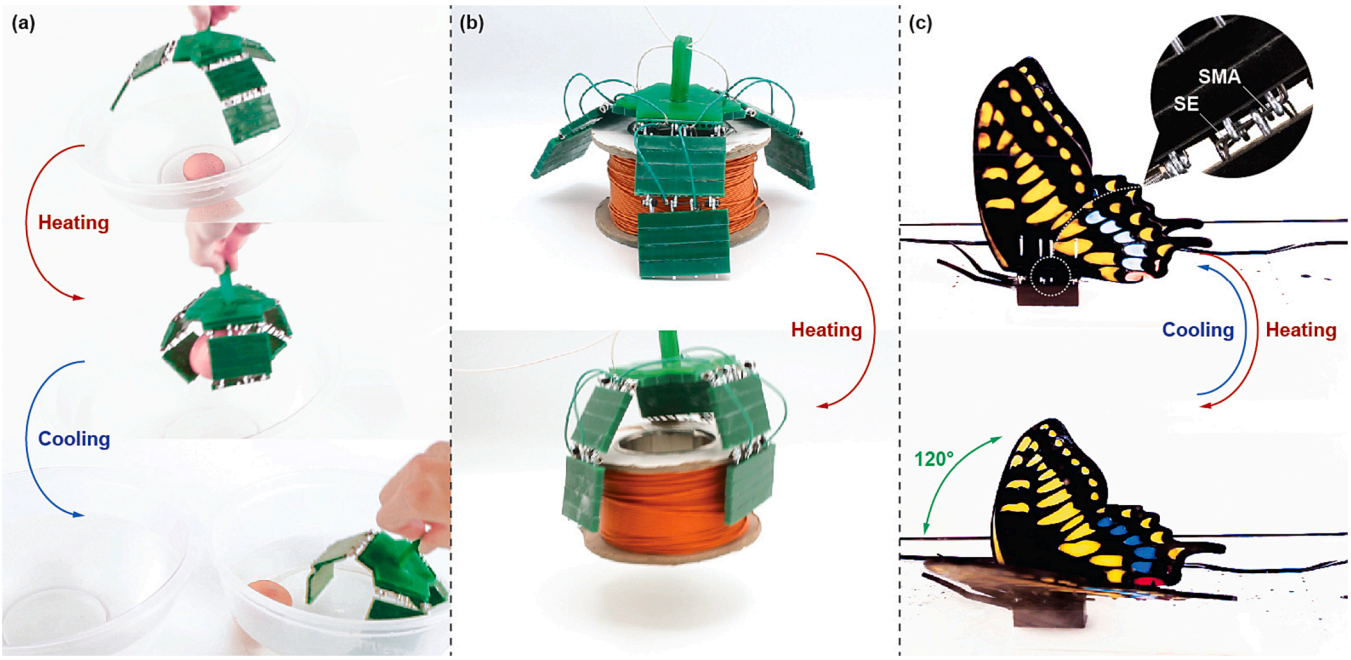

Fig. 12. Application examples. (a) and (b) A gripper constructed by 6 reversible torsion hinge actuators. It is able to grab up an egg when actuated in hot water, and release in cold water. It can also lift up a 0.6 kg wire bundle easily. (c) A butterfly demonstrator is constructed by two reversible hinge actuators.

to a value of 60° at 1.7 cm torsion length. In general, the deviation between the model predictions and experiments was seen to be 13.5 ± 8.2 %. The model is practical because it directly relates geometrical design parameters to the opening and closing angles of the hinge system. It is therefore considered valuable for scientists, engineers as well as designers.

We showed that with a hinge structure which only weighs 2 g, the actuator can generate up to 5 N when actuated. A gripper and a butterfly demonstrator were constructed to show possible application scenarios. The actuators hold potential for many fields including soft robotics, aerospace and medical surgical instruments owing to their small form factor and high actuation force.

CRediT authorship contribution statement

Qiang Liu: Conceptualization, Validation, Writing – original draft, Writing – review & editing. **Sepideh Ghodrat:** Conceptualization, Validation, Supervision, Writing – review & editing. **Kaspar M.B. Jansen:** Conceptualization, Supervision, Validation, Writing – review & editing.

Declaration of competing interest

The authors declare that they have no known competing financial interests or personal relationships that could have appeared to influence the work reported in this paper.

Data availability

Data will be made available on request.

Acknowledgements

The authors gratefully acknowledge support from China Scholarship Council. The authors appreciate technical support of Mascha Slingerland (from Applied Lab of the Faculty of Industrial Design Engineering) and Anton Lefering (from TU Delft Reactor Institute).

Appendix A. Supplementary data

Supplementary data to this article can be found online at https://doi.org/10.1016/j.matdes.2023.112590.

References

[1] B. Hannaford, J. Winters, Actuator properties and movement control: biological and technological models, in: Multiple Muscle Systems, Springer, 1990, pp. 101–120.
[2] C. Greco, et al., The evolution of mechanical actuation: from conventional actuators to artificial muscles, Int. Mater. Rev. 67 (6) (2022) 575–619.
[3] S.M. Mirvakili, et al., Niobium nanowire yarns and their application as artificial muscles, Adv. Funct. Mater. 23 (35) (2013) 4311–4316.
[4] W. Wang, et al., Soft composite hinge actuator and application to compliant robotic gripper, Compos. B Eng. 98 (2016) 397–405.
[5] X. Dong, et al., 4D printing of electroactive shape-changing composite structures and their programmable behaviors, Compos. A Appl. Sci. Manuf. 157 (2022), 106925.
[6] R. Granberry, et al., *Functionally Graded Knitted Actuators with NiTi-Based Shape Memory Alloys for Topographically Self-Fitting Wearables*, Adv. Mater. Technol. 4 (11) (2019).
[7] S. Yamamura, E. Iwase, Hybrid hinge structure with elastic hinge on self-folding of 4D printing using a fused deposition modeling 3D printer, Mater. Des. 203 (2021), 109605.
[8] Y. Liu, et al., Self-folding of polymer sheets using local light absorption, Soft Matter 8 (6) (2012) 1764–1769.
[9] Z. Liu, et al., Design, material properties and performances of a smart hinge based on shape memory polymer composites, Compos. B Eng. 193 (2020), 108056.
[10] S.M. Felton, et al., Self-folding with shape memory composites, Soft Matter 9 (32) (2013) 7688–7694.
[11] Costanza, G. and M.E. Tata, Shape Memory Alloys for Aerospace, Recent Developments, and New Applications: A Short Review. Materials, 2020. **13**(8).
[12] . Hartl, D.J. and D.C. Lagoudas, *Aerospace applications of shape memory alloys.* Proceedings of the Institution of Mechanical Engineers, Part G: Journal of Aerospace Engineering, 2007. **221**(4): pp. 535-552.
[13] H. Doty, R. Abbaschian, Structural materials: properties, microstructure and processing, Mater. Sci. Eng. A 195 (1995) 101–111.
[14] S.A. Shabalovskaya, Surface, corrosion and biocompatibility aspects of Nitinol as an implant material, Biomed. Mater. Eng. 12 (1) (2002) 69–109.
[15] Chernyshov, G., et al., Shape memory alloy wire actuators for soft, wearable haptic devices, in Proceedings of the 2018 ACM International Symposium on Wearable Computers. 2018. pp. 112-119.
[16] K. Eschen, et al., Amplifying and Leveraging Generated Force Upon Heating and Cooling in SMA Knitted Actuators, ACS Appl. Mater. Interfaces (2020).
[17] Q. Liu, et al., Shape Memory Alloy Actuators for Haptic Wearables: A Review, Mater. Des. (2023), 112264.

[18] H.-I. Kim, et al., Soft morphing hand driven by SMA tendon wire, Compos. B Eng. 105 (2016) 138–148.
[19] W. Wang, H. Rodrigue, S.-H. Ahn, Deployable soft composite structures, Sci. Rep. 6 (1) (2016) 1–10.
[20] E. Hawkes, et al., Programmable matter by folding, Proc. Natl. Acad. Sci. 107 (28) (2010) 12441–12445.
[21] Seigner, L., et al. *Bi-Directional Origami-Inspired SMA Folding Microactuator*. in *Actuators*. 20Multidisciplinary Digital Publishing Institute.
[22] H.T. Lee, F. Seichepine, G.Z. Yang, Microtentacle Actuators Based on Shape Memory Alloy Smart Soft Composite, Adv. Funct. Mater. 30 (34) (2020) 2002510.
[23] Koh, J.-s., S.-r. Kim, and K.-j. Cho. Self-folding origami using torsion shape memory alloy wire actuators. in International Design Engineering Technical Conferences and Computers and Information in Engineering Conference. 2014. American Society of Mechanical Engineers.
[24] C. Liang, C.A. Rogers, One-dimensional thermomechanical constitutive relations for shape memory materials, J. Intell. Mater. Syst. Struct. 8 (4) (1997) 285–302.
[25] S.-M. An, et al., Engineering design framework for a shape memory alloy coil spring actuator using a static two-state model, Smart Mater. Struct. 21 (5) (2012), 055009.
[26] H. Sadiq, et al., The effects of heat treatment on the recovery stresses of shape memory alloys, Smart Mater. Struct. 19 (3) (2010), 035021.
[27] Rao, A., A.R. Srinivasa, and J.N. Reddy, *Design of shape memory alloy (SMA) actuators*. Vol. 3. 2015: Springer.
[28] K. Kus, T. Breczko, DSC-investigations of the effect of annealing temperature on the phase transformation behaviour in Ni-Ti shape memory alloy, Mater. Phys. Mech. 9 (1) (2010) 75–83.
[29] Cross, W.B., A.H. Kariotis, and F.J. Stimler, *Nitinol characterization study*. 1969, NASA.
[30] Duerig, T.W., K. Melton, and D. Stöckel, *Engineering aspects of shape memory alloys*. 2013: Butterworth-heinemann.
[31] X. Huang, et al., Nanoindentation of NiTi shape memory thin films at elevated temperatures, Int. J. Smart Nano Mater. 2 (1) (2011) 39–49.
[32] M. Salehi, et al., Mechanical properties identification and design optimization of nitinol shape memory alloy microactuators, Smart Mater. Struct. 23 (2) (2013), 025001.
[33] Mabe, J.H., et al. *NiTinol performance characterization and rotary actuator design*. in *Smart Structures and Materials 2004: Industrial and Commercial Applications of Smart Structures Technologies*. 2004. SPIE.
[34] J. Mohd Jani, et al., A review of shape memory alloy research, applications and opportunities, Mater. Des. 56 (2014) 1078–1113.